Journal of Applied Water Engineering and Research, 2014
Vol. 2, No. 2, 140–156, http://dx.doi.org/10.1080/23249676.2014.981371

Flow pattern at a river diffluence at the alluvial system of the Paraná River

M.I. Morell[a,c], P.A. Tassi[b] and C.A. Vionnet[a,c*]

[a]*CENEHA – Water Resources & Engr. Dept., Universidad Nacional del Litoral, Paraje El Pozo, Santa Fe, Argentina;* [b]*EDF – Recherche & Développement, Laboratoire National d'Hydraulique et Environnement & Saint-Venant Hydraulics Laboratory, 6 quai Watier, 78401 Chatou Cedex, France;* [c]*CONICET – National Council for Scientific and Technological Research, Argentina*

(*Received 30 December 2013; accepted 23 October 2014*)

This communication presents field and numerical data depicting the flow pattern formed at a diffluence of the Colastiné River, Argentina, where one branch accesses the local harbour. The harbour has been in decline since the 1970s due to costly maintenance dredging of the access channel. The objective of this work is thus twofold: to show the persistence of the flow pattern developed at the diffluence despite recent morphological changes seen at the site, and to test a possible solution to the access channel sedimentation problem. Knowledge gained during the execution of the study helped to validate a code developed to process field data captured with two acoustic Doppler current profilers (ADCPs). The results confirm that both branches are prone to developing secondary currents. Simulations show that an engineering intervention downstream of the bifurcation can establish a self-dredging flow reversal along the access channel, turning the actual diffluence into a stable confluence.

Keywords: confluences–diffluences; helical motion; secondary currents; river bends; ADCP measurements; Telemac-Mascaret system

1. Introduction

Santa Fe City is located 476 km northwest from Buenos Aires. The city was declared "Puerto Preciso" during the Spaniard rule, forcing all ships sailing the Paraná River to stop by on their way to or from Asunción, Paraguay. It is the furthest inland harbour within Argentina for oceanic vessels. It was moved several times since the city foundation in 1573. In 1886, the city located its harbour on the Colastiné River and moved it further upstream to a new site in 1890 (pts.(a) and (b), respectively, Figure 1). Both sites were flood-prone lowlands. Therefore, an enhanced harbour surrounded by higher lands was built between 1907–1910, on its current location (pt.(c), Figure 1).

An access channel was excavated to link the port with the main channel of the Paraná River. The flow expansion created at the bifurcation between the access channel and the Colastiné River outlet induced a continuous sedimentation of the sands carried in suspension, requiring out periodic maintenance dredging of the external reach of the access channel, behind the recently formed mid-channel island (Figure 1). The harbour has been in decline since the 1970s due to this additional dredging cost. The situation did not change much with the privatization of the fluvial waterway that links Santa Fe with the Atlantic Ocean through the Paraná and the La Plata rivers. Whereas ships sailing along the waterway pay a toll to the concession company in charge of the maintenance dredging (Lievens 1997), the cost of having the access channel fully operational is still local matter.

In 1998 studies began to find a new place for the Santa Fe harbour, this time on the main channel of the Paraná River (FICH 1998). Nevertheless, there is a simple solution to the long standing sedimentation problem of the access channel mouth that has not been tested so far. It is technically feasible to sustain a bed shear stress distribution well above the sedimentation threshold values for sands by reversing the flow direction along the access channel (by closing the mouth of the South Derivation Channel, right next the access channel heading (pt.(d), Figure 1)).

The hydrodynamics of the study site is also of significant scientific interest in its own right. Diffluences can steer flow and sediment to either branch controlling the morphological development of the downstream channels (Federici & Paola 2003). Nonetheless, the development of the downstream branches is achieved through a series of interacting processes that are still poorly understood (Bolla Pittaluga et al. 2003; Kleinhans et al. 2008). Moreover, if the planar turn of the bifurcation is sharp enough, cells of secondary circulations may develop in response to the mechanical imbalance between the local elevation of the free-surface and the centrifugal force induced by channel curvature. The formation of cross-flow is thus possible if

*Corresponding author. Email: cvionnet@fich1.unl.edu.ar

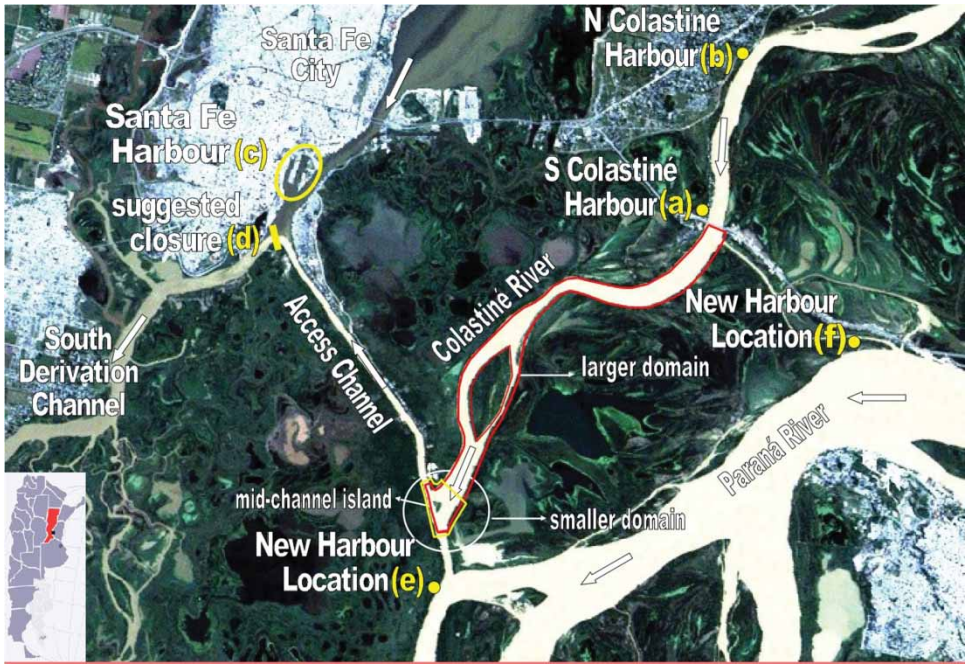

Figure 1. Location of the study site (encircled). Past, present and proposed future locations for the Santa Fe's harbour (in yellow). Satellite imagery courtesy of INPE (Instituto Nacional de Pesquisas Espaciais, Brazil).

the diffluence branches act as river bends. Whereas this response can be expected in Y-shaped diffluences (Dargahi 2004), it is far from being evident in T-shaped diffluences. In the latter case, the flow should exhibit regions of acceleration and deflection, with eventual zones of separation and reattachment with a central core of fluid moving along curved streamlines (Miori et al. 2012). Thus, the region of convectively accelerated flow should be close to the typical hydrodynamics behaviour seen along any river bend. Under these circumstances, the abundant theoretical (Rozovskii 1957; Engelund 1974; Johannesson & Parker 1989) and experimental research (Bathurst et al. 1979; Dietrich & Smith 1983) developed for open-curved flows may carry over to the study of diffluences with sharp turns.

The single cell of secondary currents usually found in flumes and in rivers scales with channel width B and water depth H, whose behaviour depends on the aspect ratio $\beta = B/H$ (Yalin 1992). Rozovskii (1957), Blanckaert and de Vriend (2004), and Kashyap et al. (2012) studied bends in flumes with aspect ratios of 13.33, 3.6, and $5.0 - 12.5$, respectively. However, there exists few field studies to date detailing the structure of helical flows driven by centrifugal forces.

Table 1 compiles values of β resulting from the field studies collected by Bathurst et al. (1979) in the river Severn (UK), by de Vriend and Geldof (1983) in the river Dommel (The Netherlands), by Dietrich and Smith (1983) in the Muddy Creek (USA), and by Dinehart and Burau (2005) in the Sacramento river (USA). For the sake of comparison, data taken by Richardson and Thorne (2001) at the Brahmaputra–Jamuna River (Bangladesh), and by Szupiany et al. (2009) at the main channel of the Paraná River (Argentina) are also included. These authors claimed to have detected secondary currents albeit at river confluences rather than in river bends. The field data show that cross-flow circulation driven by curvature develops whenever $10 \leq \beta \leq 15$.

Table 1. Some field data from rivers around the world.

River	B(m)	H(m)	β
Severn, UK (Bathurst et al. 1979)	12.0	0.90	13.3
Dommel, The Netherlands (de Vriend and Geldof 1983)	7.0	0.58	12.0
Muddy Creek, USA (Dietrich and Smith 1983)	5.5	0.50	11.0
Brahmaputra, Bangladesh (Richardson and Thorne 2001)[a]	450.0	6.00	75.0
Sacramento, USA (Dinehart and Burau 2005)	130.0	12.00	10.8
Paraná main channel, Argentina (Szupiany et al. 2009)[a]	850.0	15.00	57.0
Colastiné, Argentina (this study)	130.0	10.00	13.0

[a]*Confluences*, whose hydrodynamics is not necessarily equivalent to those observed on river bends (Rhoads and Kenworthy 1998).

In tune with the foregoing issues, this paper is concerned with the flow pattern developed at the diffluence of the Colastiné River when rejoining the Paraná main channel, an aim achieved through field measurements and 2D and 3D numerical simulations. The objective of this work is thus twofold: to show the persistence of the flow

pattern developed at the diffluence despite recent morphological changes experienced by the site, and to test a simple solution to the chronic sedimentation problem seen at the access channel mouth.

Knowledge gained during the execution of the study helped to refine and validate a computer code developed to process field data captured with two acoustic Doppler current profilers (ADCP). Both, field and numerical results show that the two branches of the diffluence act like true river bends, and consequently are prone to developing secondary currents. Field data show this is indeed the case along the right branch, which was the only systematically measured branch. It remains to extract the results from the open-source Telemac system (Telemac-Mascaret Modelling System 2014), following the field data treatment, in order to assess the predictive code capability to reproduce the observed secondary currents.

The following section describes the study site and the collected data, including a brief description of the in-house software developed to treat the field data. Then, a description on how and why the right downstream branch of the diffluence acts as a river bend is presented. Finally, a qualitative comparison between simulated results and observed cross-flow data is given next, to close with the proposed engineering solution to the access channel sedimentation problem.

2. Materials and methods

2.1. Study site

The incoming flow from the Colastiné experiences a sharp turn at the access channel inlet (Figure 2(a)), which makes it prone to centrifugal effects and, therefore, susceptible to developing secondary currents. Table 2 summarizes the main parameters either collected or set-up during the fieldworks: the river discharge Q and free-surface elevation z_w corresponding to low-medium flow conditions, the vessel velocity V, and the ADCP sampling volume and time, Δz and Δt, respectively.

In the occassion of the field campaign of 2004, the existing mid-channel bar was submerged albeit the water depth was too shallow for sailing over it. On the contrary, the river stage was higher during the fieldwork of 2006 making it possible to collect data over the sandbar. Figure 2(b) shows the river water levels on the field trips dates, and during the Landsat imagery dates used to fill the late evolution of the riverbanks.

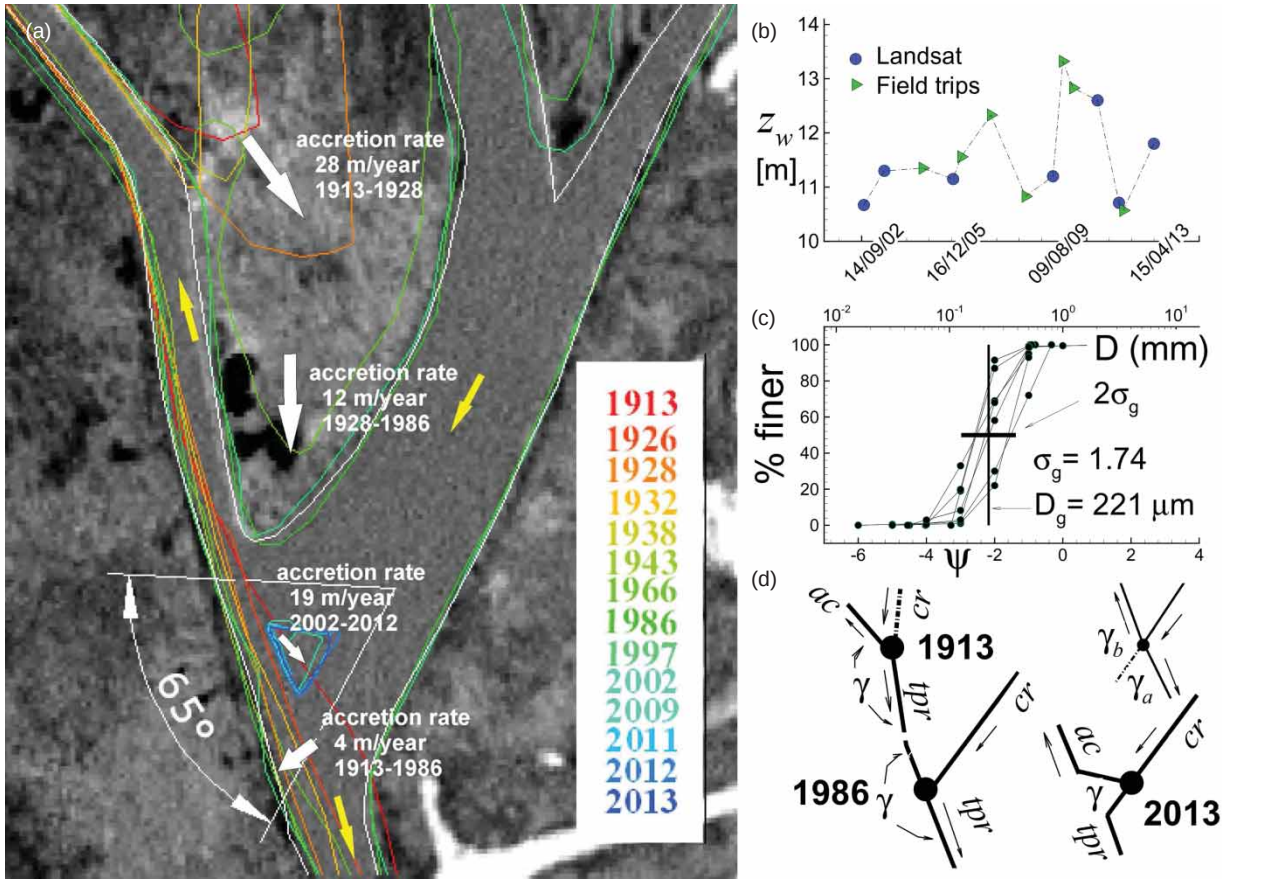

Figure 2. (a) Morphological evolution of the study area, (b) water levels with Table 2 and Landsat imagery dates, (c) grain size distribution, and (d) 1D evolution sketch of the bifurcation node since 1913 (*ac*: access channel, *cr*: Colastiné River, *tpr*: to Paraná River). Satellite imagery courtesy of CONAE (National Agency of Space Activities, Argentina).

Table 2. Fieldwork parameters: z_w: water stage above datum at Santa Fe harbour, Q: access channel discharge, V: vessel velocity, Δz: ADCP bin size and Δt: ADCP sampling time interval.

Date	z_w (m)	Q (m^3/s)	V (m/s)	Δz (m)	Δt (s)
2004[a]	11.23	856 ± 98	0.72	0.90	20.00
2006[a]	11.51	917 ± 101	0.67	0.50	5.00–10.00
2007[a]	12.16	663 ± 116	1.36	1.10	10.00
2008[a]	10.78	622 ± 119	1.15	0.75	10.00
2009[a]	13.27	1083 ± 126	0.65	0.90	10.00
2010[b]	12.78	1085 ± 63	1.52	0.25	0.59
2012[b]	10.57	595 ± 14	1.15	0.25	0.59

[a]Sontek RiverSurveyor 1000 kHz.
[b]TRDI Río Grande 1200 kHz.

The field site is within the alluvial system of the Paraná River, a large low gradient sandy river with a free-surface slope ranging between 3 and 5 cm per kilometre (i.e. $[3-5]\times10^{-5}$). The Colastiné is an anabranch of the Paraná River with riverbanks composed of a 4–6 m layer of clay and silt overlying coarse sands (Iriondo 2007). It is a typical meandering river with an approximated average water depth, channel width, and discharge of 6 m, 600 m, and 1700 m^3 s^{-1}, respectively. About 80–85% of the Colastiné and Paraná sediment transport is wash load made of silts and clays barely found in measurable quantities in the bed (Amsler et al. 2005). The rest is bed material made of fine and medium sands predominantly carried in suspension. Figure 2(c) depicts several particle size distribution of bed material collected at the study site. The samples are characterized by an average geometric mean size and standard deviation $D_g = 221\,\mu$m and $\sigma_g = 1.74$, respectively.

Figure 2(a) summarizes the morphology variations of the site in the last 100 years according to data retrieved from old navigation charts and recent Landsat imagery. The accretion rate of the wedged-shaped floodplain created between the former Colastiné course and the newly excavated access channel was about 28 m/year between the years 1913–1928. By contrast, the wedged evolved into a tongue-shaped floodplain at the slower rate of 12 m/year in the years 1928–1986 and remained stable since then. The tracked riverbanks displacements yielded an average accretion rate of 19 m/year for the head of the mid-channel island while the "horizontal bar" of the original T-shaped diffluence has remained almost unchanged since 1913, with an accretion rate of 4m/year at most. The formation of the tongue-shaped right floodplain was part of larger scale processes attributed to the climate variability of the twentieth century (Amsler et al. 2005).

Consequently, there seems that whereas the riverbanks experienced a long-term adaptation processes, the recent growth of the mid-channel island formed at the bifurcation obeys short-term processes. The rapidly evolving mid-channel island conforms with the local divergent planform of the diffluence. Recent changes in the Colastiné hydrology could have contributed to the island formation. The mean channel width along the Colastiné has decreased an average of 16–21% in the years 1977–2009 in response to a mean river discharge decline of about 16–26% (Amsler et al. 2005; Ramonell 2012). If the mid-channel island formation is the result of the sudden loss of the river transport capacity at the bifurcation, to the river changing hydrology, or a combination of both is beyond the scope of this work. Resolving these processes imply having data across a wide range of spatial and temporal scales, an extremely difficult task due to the required resources as well as the need to count with an accurate record of topographic data.

The typical one-dimensional (1D) description of a river bifurcation consists of three branches linked through a node. In this context, the bifurcation angle is defined by the centerlines of the two downstream branches relative to the upstream channel orientation ($\gamma = \gamma_a + \gamma_b$, Figure 2(d)). Figure 2(d) sketches the tracked morphology evolution of the bifurcation node since 1913. The newly excavated access channel created a Y-shaped diffluence of the Colastiné River with an initial bifurcation angle $\gamma \simeq 152^\circ$. With time, the Colastiné swiftly moved south towards its current morphology accompanying the evolution of the main channel of the Paraná itself (Amsler et al. 2005). By the mid-1980s, the bifurcation had evolved to an almost T-shaped diffluence with an angle $\gamma \simeq 189^\circ$. The system remained unchanged for years till the turn of the century, when the mid-channel bar formed right upstream of the diffluence eventually began to emerge. The mid-channel bar remained under or above water depending on the river hydrology (Figure 2(b)). From 2008 onwards, the sandbar was colonized by vegetation and recently evolved to a mid-channel fluvial island used for livestock grazing by local inhabitants. Nowadays, the hydrodynamics diffluence is driven by the mid-channel island conforming to a Y-shaped bifurcation with a new angle $\gamma \simeq 65^\circ$.

2.1.1. *A note on bifurcation stability*

River bifurcations behave as switches that steer the flow and sediment partitioning into the two downstream branches (Federici & Paola 2003). Bifurcations are "stable" if both branches remain open through time, and "unstable" whenever one of the two downstream branches tends to be abandoned (Bolla Pittaluga et al. 2003). Channels upstream of stable bifurcations are straight, widening towards the bifurcation node. Burge (2006) reported that bifurcations characterized by greater angles may be inefficient for an even distribution of water and sediment between both anabranches. In contrast, bifurcations with smaller angles may remain stable by dividing water and sediment more evenly (Federici & Paola 2003).

Even though the bifurcation seems to be stable, the external reach of the access channel (behind the mid-channel island) requires periodic maintenance dredging to

keep the waterway operational. It is likely that the recent formation of the mid-channel island head that divides sediment and water into the downstream branches can also contribute to the stability of the bifurcation. The accretion rate of the mid-channel island head was about 19m/year in the period 2002–2012, reducing the former bifurcation angle γ from 189° to the actual 65°, close to the stable range of 40–60° reported by Federici and Paola (2003).

2.2. Velocity measurements

Data captured with ADCP are routinely used to study 3D flows, and the trend is to repeat transects along linear routes to resolve weak cross-stream velocities (Dinehart & Burau 2005). In this work, two different ADCP has been systematically used in the study site; a 1000 kHz RiverSurveyor manufactured by Sontek and a 1200 kHz Workhorse Río Grande manufactured by Teledyne RD Instruments (TRDI). The proprietary software packages *RiverSurveyor* and *ViewADP* for the Sontek ADCP, and *WinRiver* II for the TRDI ADCP were used for data acquisition and integration with positional information from satellite data. However, and due to an ongoing effort to develop a set of in-house routines to process the field data, the present work restricts the analysis regarding the 3D structure of the flow velocity to data captured with the Sontek ADCP, whereas flow discharge data analysis is limited to the TRDI ADCP measurements. A full description of the in-house codes is beyond the scope of this work.

Water velocity and bathymetry data were collected using one of the ADCP in parallel with a differential Global Positioning System (dGPS) receiver with Real-Time Kinematic (RTK) technology. The RTK system, sampling at the rate of two positional points per second, provided accuracies of ± 0.02 m in planar and ± 0.04 m in vertical direction. A second serial port to connect a digital 210 Hz Raytheon single beam echo sounder was attached to the on-board computer during the surveys.

The down-looking ADCP was mounted on the side of a fibreglass-hull vessel of 6.4 m in length, when a combined bathymetry and flow velocity field survey were carried out using the moving boat methodology (Muste et al. 2004). For most of the field works, the Sontek ADCP was set to a cell size and sampling interval (or ensemble) of 0.75 m and 10 s, respectively, with a boat velocity preferably below 1.5 m/s to obtain reasonably accurate flow measurements (Szupiany et al. 2007). The TRDI was set up to work under water mode 1 with a bin size of 0.25 m and a sampling frequency of one ensemble every 0.59 s (Table 2).

Three types of single-beam bathymetry data sets were collected during the field works spanning the years 2004–2012. One set of data, designed to guide data-collection operations, corresponded to survey lines covering the study area with an approximate separation interval of 50 m each. In addition, a separate set of navigation lines, skewed to the approximately equally spaced transects, were planned to provide independent measurements of precision and bias. These skewed lines served later on as an independent basis to test the adequacy of the interpolated digital bed elevation model (DEM). A mean depth of 7 m at the navigation channel, and about 3.5 m at the outlet of the Colastiné River, with a mean channel width of 130 m and 600 m, respectively, were determined during these measurements. A scour hole with a bed elevation of −6.5 m was found on the right branch, a short distance downstream from the point of maximum curvature, in comparison with the ground elevation of about 14 m of the nearby inner bank (Figure 3(a)).

The third set of bathymetry data were pick-up along transects aligned with rays departing from a virtual centre of curvature, pinpointed over the land surface on the right -inner- bank side. These rays were drawn in advance to all field works, and the centre of curvature was determined by fitting a circle to the river planform of the inner bank. The helmsman then followed the drawn transects as closely as possible by tracking the vessel position in real-time with the dGPS. Nevertheless, in order to verify if the adopted cross-section orientations were supposedly perpendicular to the primary flow direction, two floats made with a 1.8 m long and 5 cm-diameter PVC tube and equipped with Blue-tooth GPS (Garmin 10X) were used to identify depth averaged particle paths at the sharp turn of the navigation channel inlet. Data from the GPS were logged at 2 s interval onto a portable computer (with enhanced Blue-tooth communication of up to 100 m reach) by using standard navigation software. The floats were released just 100–150 m upstream of the Colastiné River's outlet on 18 March 2009, prior to the field survey with the TRDI ADCP.

2.3. Data analysis

2.3.1. Digital bed elevation model – DEM

The ADCP internal compass and tilt sensor (roll/pitch) referred water velocities components in terms of East-North-Up (ENU) coordinates. The collected bed elevation data in ENU coordinates, corrected by the magnetic declination bias, were later converted to Transverse Mercator (TM) coordinates with the formulas given by Snyder (1929), with the new World Geodetic as the reference system (WGS 84). For Argentina's Gauss-Krüger (TM) coordinates, the origin is the intersection of the South Pole with the central meridian of each band, and with a northing of zero. This procedure was packed in a module, part of a bundled software written in fortran 95 to merge field data with point and polyline data from complementary sources (river banks elevations, borderlines around inner islands, etc.). The bundled comprises the SMS (2000), the visualization tool Tecplot (2011), and a set of in-house routines described in Vionnet (2010).

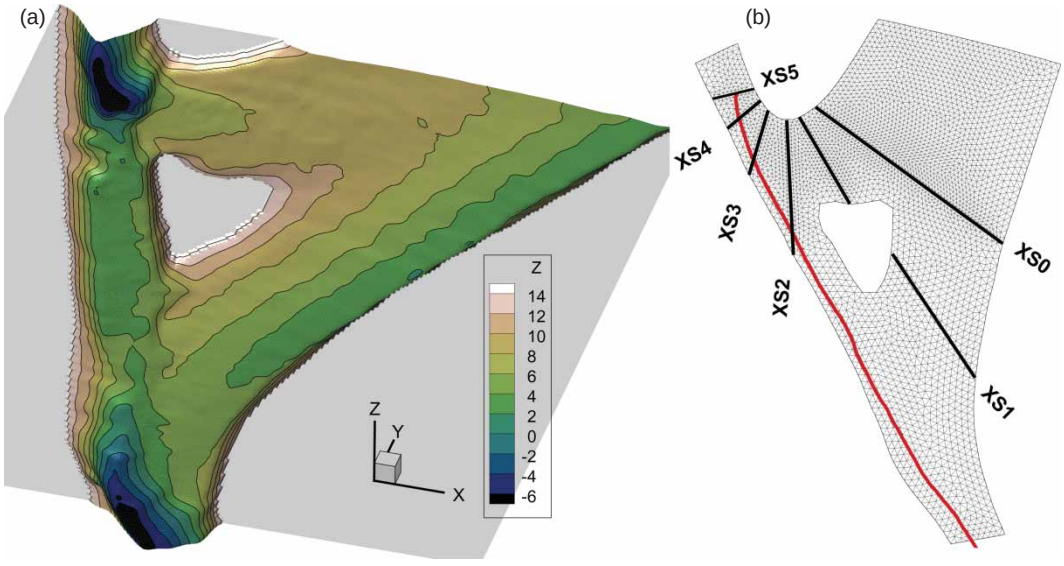

Figure 3. (a) DEM of the study site (ground elevation in metres), (b) Finite element mesh and surveyed cross-sections (XS) – red line: boat path followed during the water surface elevation survey.

This topographic data manager tool allows to alter the outcome of the interpolation from the scatter data using different criteria, which may guide the user with the continuous assessment of the DEM-generation process. An adaptive tessellation of the domain is then constructed with a Delaunay triangulation from the scatter point set. This triangular irregular network, linking each scatter point, allows the interpolation of elevation data using linear base functions onto a regular grid, whose steps-size are defined by the user. The algorithm defines automatically which node of the regular grid is inside or outside the computational domain, information used later to pass a 2D Laplacian kernel to smooth out the resulting bed elevation interpolation. This is because the DEM should represent the bare surface of the river bed with a smooth transition between the bed and riverbanks whenever possible, in order to avoid convergence difficulties nearby the boundaries of the computational domain due to contradictory data between bed elevation and local water depth.

A first DEM was generated with bathymetry data collected only with the echo sounder, whereas the final DEM was produced with data captured with the echo sounder between 4 and 5 May 2010 (Table 2), and depth data estimated through the four-beam readings of the ADCP TRDI, corrected by roll and pitch with the aid of the Velocity Mapping Toolbox (VMT, Parsons et al. 2013). Figure 3(a) depicts the DEM so obtained.

2.3.2. *ADCP data*

Occasionally, reported results seem to be vague and open to different interpretations depending on the method used to extract secondary currents from the field data (Lane et al. 1999; Rhoads and Kenworthy 1999). Despite this still ongoing controversy within the scientific community, the vast majority of researchers refer to the so-called Rozovskii method (see Rozovskii 1957, p. 138) to infer secondary motion. The Rozovskii procedure isolates the excess (or deficit) of the transverse velocity component relative to the respective depth-averaged value on any vertical profile. The method accounts for a rotation of the planar velocity vector with respect to the direction of the depth-averaged velocity vector. However, the procedure depends upon having zero net secondary discharge at the vertical, a condition normally used to close the mathematical problem posed by the set of governing equations (Engelund 1974), albeit unrealistic in practical situations.

Dinehart and Burau (2005) proposed a two steps method to isolate secondary currents: first, a bend-crossing plane of velocity vectors from ADCP data are derived, and second, elements of the backscatter intensity planes are used to guide an interactive alignment of the averaged velocity grids previously obtained. They found the bend-crossing plane through a section-straightening procedure, where the velocity ensembles are spatially translated to a straight line defined by a mean crossing line fitted along multiple transects.

The procedure adopted here for post-processing the field data involve two steps: the use of proprietary software in the first place and then in-house routines to get the transverse velocity field. In other words, filtered 3D flow data were first exported into spreadsheet files written in ASCII format with the proprietary program *ViewADP* (Sontek 2004) or *WinRiver* II (TRDI 2007), and later loaded into a fortran 95-based software package called *read_aDcp* for further processing and visualization. The procedure *after_read_aDcp* allows users to integrate primary and secondary velocities from one or more surveyed

cross-sections with the DEM, in turn generated with the routines described in Vionnet (2010).

The 3D velocity field data are projected with a procedure similar to that proposed by Dinehart and Burau (2005). Secondary currents were computed with (or without) the zero net cross-stream discharge constraint. The code decomposes both the horizontal-two-dimensional or depth-averaged (2DH) velocity field, and the full 3D vectors into tangential (along the cross-wise plane) and normal (along the streamwise plane) components of the absolute velocity relative to the ground, with the addition of the up component for the 3D case. Finally, both the tangential and up components define the vertical-two-dimensional (2DV) representation of the flow field along the projected cross-stream plane, in turn located through an orthogonal least-squares fit to all trajectories navigated by the vessel during the surveys.

2.4. Numerical solutions

2.4.1. Numerical engine

The suite of numerical codes used in this work belongs to the open-source Telemac-Mascaret system (Hervouet 2007; Telemac-Mascaret Modelling System 2014), currently developed by the research and development department of Electricité de France (EDF) and the Telemac Consortium. The Telemac-3d module solves either the hydrostatic or non-hydrostatic continuity and the time-averaged Navier–Stokes equations with a finite element discretization fully parallelized with the message passing interface paradigm.

The hydrostatic approximation consists on neglecting the vertical acceleration, diffusion and source term in the momentum equations. The non-hydrostatic approximation is based on the pressure decomposition into hydrostatic and hydrodynamic parts, allowing an accurate computation of the vertical velocity, which is coupled with the whole system of equations. The solution steps of the hydrostatic 3D version are: (i) computation of the velocity field by solving the advection terms; (ii) determination of a new velocity components by taking into account the diffusion and source terms (intermediate velocity field); (iii) computation of the water depth from vertical integration of the continuity and momentum equations by excluding the pressure terms; and (iv) determination of the vertical velocity w from the continuity equation and computation of the pressure step by the Chorin method (Hervouet 2007).

2.4.2. Finite element meshes

The reasons why the finite element method is so successful for studying environmental problems are well known: local character of the approximation functions, ability to treat natural boundary conditions, and ease in handling complex geometrical domains. However, the generation of an adequate discretization mesh and the estimation of the solution error are in general difficult tasks, particularly over complex 3D domains.

The so-called *a priori* error estimate decides how the computed results deviate from the exact solution supplying information on convergence rates, but is unable to deliver quantitative or qualitative error information. *A posteriori* error estimates, based upon the computed solution, provide more practical accuracy appraisals (Babuska & Rheinboldt 1978). This estimation seeks to evaluate the error in some specific measure, where the idea is to refine the mesh such that the errors are "equally" distributed over the computational mesh. Nevertheless, this error measure is somehow too abstract and does not provide users with specific features of the solution.

Consequently, the users usually base their final decision on similar, earlier computations. A simple rule of thumb is to increase the number of elements to reduce its average size Δ until the results of successive computations show no perceptible difference.

All triangular finite element meshes used here were produced with SMS (2000) with the embedded DEM and later exported into the binary Telemac format (called selafin; Mourad, 2011, personal communication). The meshes were fitted along external and internal boundaries where flow quantities were available (Figure 3(b)). The 3D finite element mesh was later obtained by extruding each linear triangle along the vertical direction into linear prismatic columns that exactly fit the bottom and the free-surface. In doing so, each column can be partitioned into nonoverlapping layers, requiring that two adjacent layers comprise the same number of prisms.

3. Results

3.1. Field data

3.1.1. Independent computation of river discharge

Due to intrinsic operational limitations, the ADCP is unable to measure near the bed, banks, and free-surface (Simpson 2001). For example, the Sontek ADCP employed has a profiling range capability of 1.2–40.0 m, and a cell-size ranging between 0.25 and 5.0 m with a minimum blanking distance of 0.7 m. The distance from the water surface to the centre of the first bin was about 1.3 m approximately [$= 0.7$ m (blanking distance) $+$ 0.2 m (probe submergence) $+ \Delta z/2$ (see Table 2)]. The blind distance at the top layer and the "contaminated" bottom layer by side-lobe interference rendered between 55% and 15% of unmeasured depth for water columns located in shallow and deep zones, respectively. However, as it is shown later, the bulk of moving water scanned by the ADCP was large enough to capture cells of secondary circulation.

The mentioned limitations are overcome by the manufacturer through the utilization of extrapolation methods, which covers from the one-sixth power-law estimation

technique to fit the vertical velocity profile within the inner portions of the cross-section to the ratio interpolation procedure to infer the near-shore flow rates (Sontek 2004; TRDI 2007).

Contrary to these techniques, used to infer the flow discharge in real-time situations (Simpson 2001), an independent calculation based on different assumptions was developed to test the in-house code. This *a posteriori* estimate is based upon a rather crude approximation of the flow profiles along the gauged area of the cross-section as well as on the ungauged portions (free-surface, bed and banks). Nevertheless, if the 3D structure of the loaded velocity field is correctly handled by the in-house code, these new flow discharge estimates should not be far from the values reported by the proprietary software.

It suffices to note that whereas the river discharge measured on 4–5 May 2010 (Table 2), estimated with the software *WinRiver* II (TRDI 2007) was 1085 m^3/s on average with a fractional standard deviation of about 5.8%, the computation with *read_aDcp* yielded a mean value of 1100 m^3/s with a standard deviation of 6.1%. Sixteen values of discharges measured along cross-sections XS1, XS3, XS4, and XS5 were selected (see Figure 3(b) for reference locations). The values measured on cross-section XS2 were ruled out because this transect is affected by recirculating flow nearby the left riverbank. Both results, the estimated with the proprietary software and the approximated with the in-house code have similar frequency distributions, with a median of 1100 m^3/s (see appendix).

It is seen that the river discharge values obtained with the in-house code bears favourable technical comparison with the values produced by the proprietary ADCP software. The comparison can be favourable only if the 3D velocity field is correctly uploaded by the code. In brief, the in-house code handles the field data in a manner consistent with the proprietary software and, therefore, it can be deemed appropriated for further processing, for example, the isolation of secondary currents.

3.1.2. *Cells of secondary circulation along the right branch of the diffluence*

The experience accumulated when studying helical motion (Rozovskii 1957; Engelund 1974; Bathurst et al. 1979; Johannesson & Parker 1989) can be well suited to understand the present flow behaviour as long as the diffluence branches behave as river bends.

Figure 4(a) plots the measured float paths along the diffluence showing a clear flow partition upstream of the two river branches, with a downstream zone where the water is either stagnant or circulating weakly (behind the mid-channel island). This pattern is reproduced in Figure 4(b), which depicts the numerical results of a 2DH calculation obtained with Telemac-2d. There is a clear correspondence between the observed float paths and the computed streamlines of the depth-averaged flow.

Some characteristic flow features along the right branch of the diffluence are observed in Figure 4; (i) the size and shape of the stagnant water zone behind the mid-channel island, which bounds the water motion along the right branch in such a way that it looks like an open-water pipe elbow flow, (ii) the downstream extension of the detached flow behind the vortex of vertical axis formed near the curve apex; an unusual flow situation barely found on the alluvial system of the Paraná River (somehow showing the artificiality of the channel morphology, excavated at

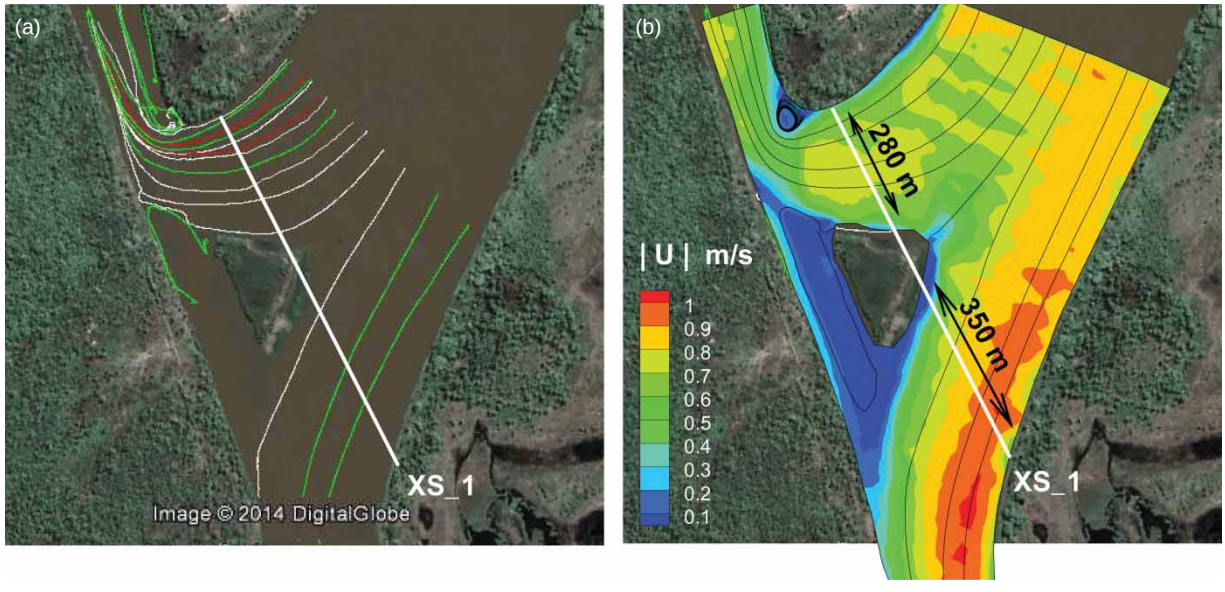

Figure 4. (a) Float paths, (b) Streamlines of the 2DH results of Telemac-2d. Source: Google Earth

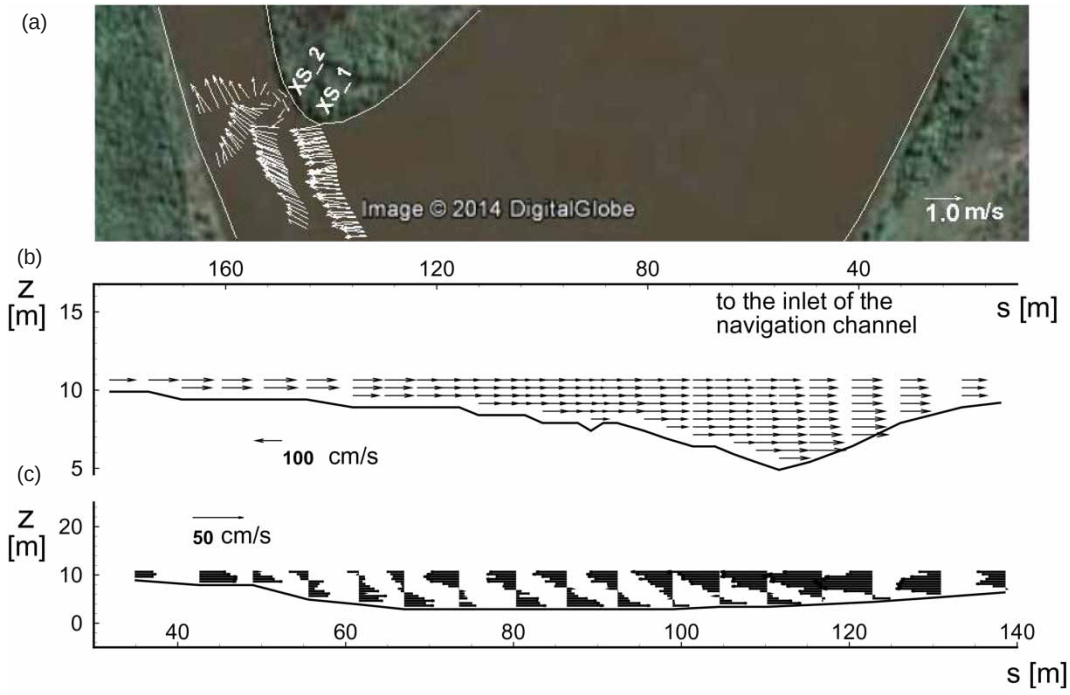

Figure 5. 2004 Sontek ADCP: (a) *ViewADV* 2DH flow vectors, Source: Google Earth, (b) *read_aDcp* 2DV flow field on right branch of XS1 (acces channel discharge: 905 m^3/s), (c) *read_aDcp* 2DV flow field on XS2.

the beginning of the twentieth century), (iii) the convergence of neighbouring streamlines as the flow approaches the curve apex, not only in response to curvature effects but also enhanced by an effective cross-section reduction due to the vortex presence. It seems then that the curved flow along the right branch should be prone to the formation of secondary flow. This distinctive flow feature should be embedded in both the numerical results and the field data, where the former depends on the ADCP proprietary software, and to a lesser extent, on the used in-house code.

The proprietary *RiverSurveyor* software (Sontek 2004) handles depth-averaged data across the measured transect without further processing. Thus, after conversion of geographical positions to TM (Gauss–Krüger) coordinates, the information can be readily exported onto georeferenced satellite images of the study site for further analysis. Few transects with the 2DH velocity field measured during the 2004 and 2006 field works (see Table 2) are depicted in Figures 5(a) and 6(a). A clear flow separation just downstream of the inner bank apex is observed in both field data, which surely alters the size and shape of the secondary circulation cell.

In order to analyse the 3D structure of the flow field, it was necessary to resort to the in-house code. Upstream of XS2 it is possible to observe two well differentiated flow behaviour. Figure 5(b) shows that the streamwise acceleration and deceleration the flow must undergo at the outer and inner banks, respectively, along XS1 are so significant that a net unidirectional flow in the crosswise direction from outer to inner regions must set up for mass continuity reasons.

A word of caution is required here: Figures 5(b) and 6(b) correctly depict cross-section XS1 from left to right riverbanks where the cumulative distance *s* starts from zero at the first gauged water column. Data taken on 2006 show a well-defined flow partition above the sandbar (Figure 6(b)), in coincidence with the field and numerical data shown in Figure 4. A left branch width of about 350 m is consistent in both Figures 4(b) and 6(b). Thus, Figure 5(b) depicts the right branch of XS1 only while Figure 6(b) depicts the whole XS1. The difference in the bathymetry shape is because the boat path surveyed on 2004 was closer to the scour hole present at the curve apex.

Finally, the single cell of secondary motion is clearly seen in both Figures 5(c) and 6(c), captured along XS2 during the field works of 2004 and 2006, respectively. The secondary circulation is rather intense, with transverse velocities on the order of 0.40 m/s, which represents about 40–50% of the primary flow component.

3.2. Numerical simulations

3.2.1. Boundary conditions and mesh independency test

At the sidewalls, the velocities tangential and normal to the boundary were set equal to zero (no-slip condition). At the outlet boundaries, the normal gradients of the flow velocity were set equal to zero, whereas a free-surface elevation of 10.545 m and 10.526 m at the left and right downstream branches, respectively, were imposed. The

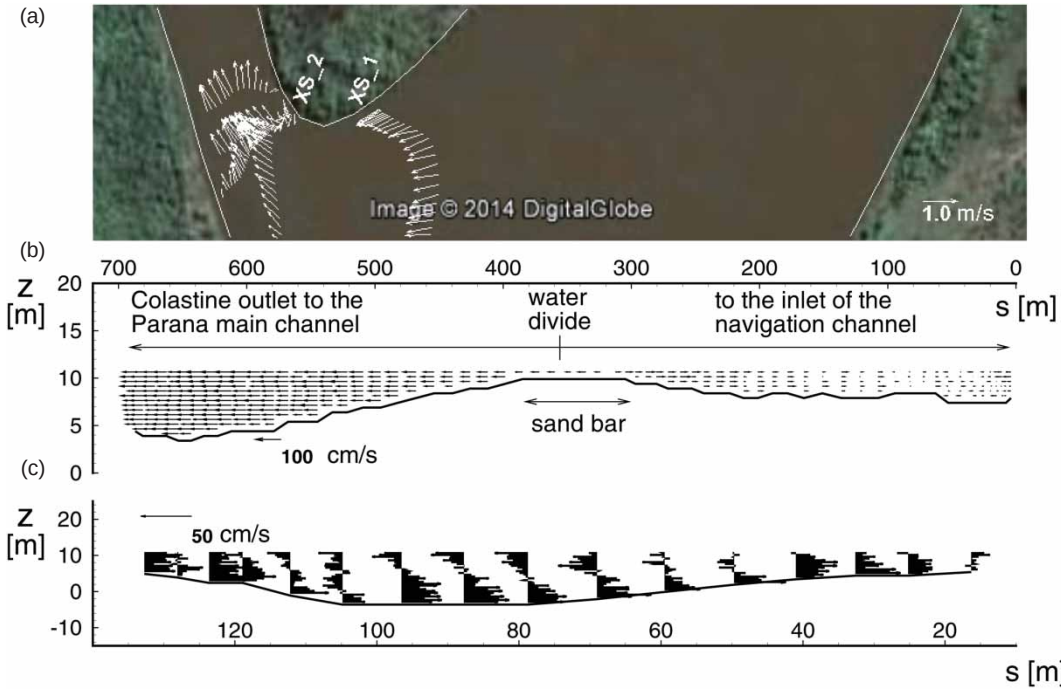

Figure 6. 2006 Sontek ADCP: (a) *ViewADV* 2DH flow vectors, Source: Google Earth, (b) *read_aDcp* 2DV flow field along the whole XS1 (acces channel discharge: 967 m^3/s), (c) *read_aDcp* 2DV flow field on XS2.

inflow boundary was fixed at $Q = 1629\,m^3/s$, and located far upstream to avoid affecting the solution in the region of interest. The field measurements yielded a closure error less than 1% in terms of river discharge ($Q_{right} = 595\,m^3/s$ and $Q_{left} = 1044\,m^3/s$). These data were measured during the fieldwork of 2 March 2012.

The generation of adequate meshes with successive halved elements is impossible when unstructured mesh generators are used to discretize the geomorphology depicted in Figure 1. Therefore, and in order to circumvent the limitations mentioned in Section 2.4.2, four meshes were generated with decreasing "mean" element size Δ according to

$$\Delta \simeq \sqrt{\frac{2\Omega}{N_e}}, \tag{1}$$

where Ω is the area of the computational domain and N_e the number of elements (N_n is the number of nodes (Table 3)). The first three meshes extended over the larger domain while the fourth mesh overlapped the shorter computational domain (see Figure 1 for details). The objective was twofold; to show that solutions computed on successive meshes display no perceptible difference albeit converging to a final state, and to infer the hydraulic gradient and the proper boundary conditions of the incoming flow into the smaller domain (Figures 1 and 3(b)).

All computations were performed over unstructured triangular meshes with 5 layers but the finer, where 15 layers were used instead. The adequacy of the results was judged on the basis of the computed flow discharge at the diffluence. Table 3 clearly shows that when the discretization is fine enough, the computed results can be considered mesh insensitive. The final flow partition of 585 m^3/s and 1044 m^3/s is well within the uncertainty range around the mean value of the measured river flow rate (see Table 2 and appendix).

For a given initial condition consisting on a constant water surface elevation and velocity components equal to zero, the steady state was reached after about 100,000 time steps of 0.1 s, corresponding to a physical time of about 2 hours 46'. When ran on eight processors of a Z600 HP workstation, the typical elapsed time to achieve convergence was on the order of 35'.

The numerical simulations were performed with a roughness-length representation based on the Nikuradse coefficient $k_s = 0.01\,m$ and with a constant turbulence model with eddy viscosity coefficient $\nu_t = 1.0 \times 10^{-5}\,m^2/s$. Different values of the hydraulic resistance height k_s were used to adjust the observed water surface slope in the streamwise direction. The adopted value of $k_s = 0.01\,m$ yielded the best fit between the observed and computed hydraulic gradient (in both computational domains, large and short). The values for ν_t were selected after the recommendations of Vionnet et al. (2004).

3.2.2. *The 3D flow structure*

The right branch of the diffluence exhibits a strong asymmetry of the bed topography. The flow along this branch

Table 3. Mesh independency test.

Mesh	N_n	N_e	Layers	Prisms	Δ [m]	Q_l [m^3/s]	Q_r [m^3/s]
1	1006	1585	5	7925	74	994	635
2	2354	4083	5	20,415	46	1056	573
3	23,224	44,534	5	222,670	15	1041	588
4	3380	6623	15	99,345	13	1044	585

Note: Q_l and Q_r stand for Q_{left} and Q_{right}, respectively.

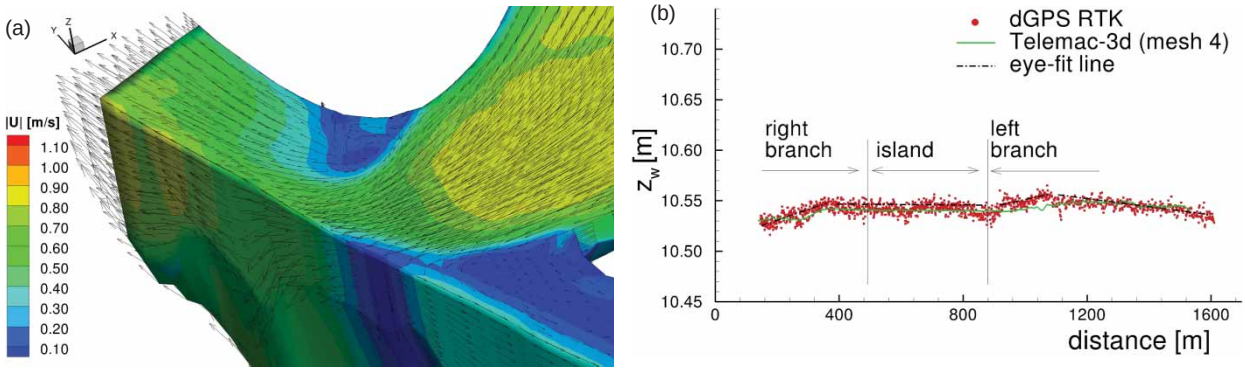

Figure 7. (a) View of the 3D flow field (measured discharge at the access channel inlet: [588–602] m^3/s (see Table 2), simulated: 585 m^3/s (see Table 3)); (b) Free-surface along the boat path of Figure 3(b).

develops zones of acceleration, stagnation, deflection, separation, and reattachment (Figures 4(a), 5(a), and 6(a)).

Figure 7(a) depicts the 3D velocity field along the edges of the computational domain nearby the outflow boundary representing the inlet to the access channel. The numerical solution captures the area of stagnant water behind the island, the vertical axis vortex at the curve apex of the inner bank, and the detached flow downstream of it. The contour map embedded in Figure 7(a) reflects the module of the 3D velocity field, in m/s.

The size and location of the vortex shown in Figure 7(a) are in fairly well concordance with the drawn float paths and with the ADCP measurements (Figures 4(a), 5(a), and 6(a), respectively). The formation of the separation zone deviates the flow towards the left bank, at the inlet of the access channel. Nonetheless, the size of the detached flow area behind the vortex of a vertical axis seems to be better captured by the 2DH simulation (Figure 4(b)) rather than by the full 3D solution. Similar effects have been noted by Lloyd and Stansby (1997) when comparing 2D and 3D shallow-water numerical solutions of the wake formation behind models of conical islands with laboratory measurements.

The longitudinal profile of the free-surface shown in Figure 7(b), whose trace is detailed in Figure 3(b), reflects part of the flow behaviour along the diffluence. The free-surface is flat behind the mid-channel island, in coincidence with the zone of stagnant water, and falls sharply on both extremes towards the inlet of the access channel and the main-channel of the Paraná River. There is a concentrated jump when the water surface, elevated by

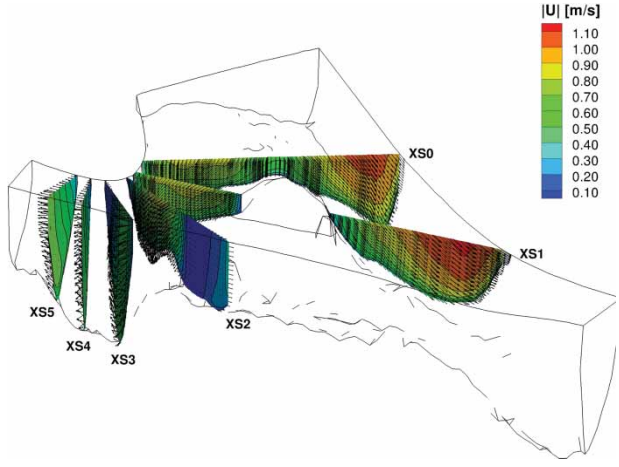

Figure 8. Computed flow patterns at surveyed XS.

the centripetal effects on the outer edge of the left branch, meets the area of the flat surface behind the island. This area of flat free-surface behaves like a rigid body since it plays the role of the missing channel wall on the outer bank. There is a clear correspondence between observed data and numerical results.

Figure 8(a) shows the numerical results along the selected surveyed cross-sections (XS), numbered from 0 (XS0) at the upstream inlet boundary to 5 (XS5) towards the downstream boundary within the access channel (see Figure 3(b) for surveyed XS locations).

The XS2, a bit downstream of the diffluence, exhibits a flow pattern compatible with a cell of secondary circulation with transverse velocities on the order of 0.40 m/s, that is,

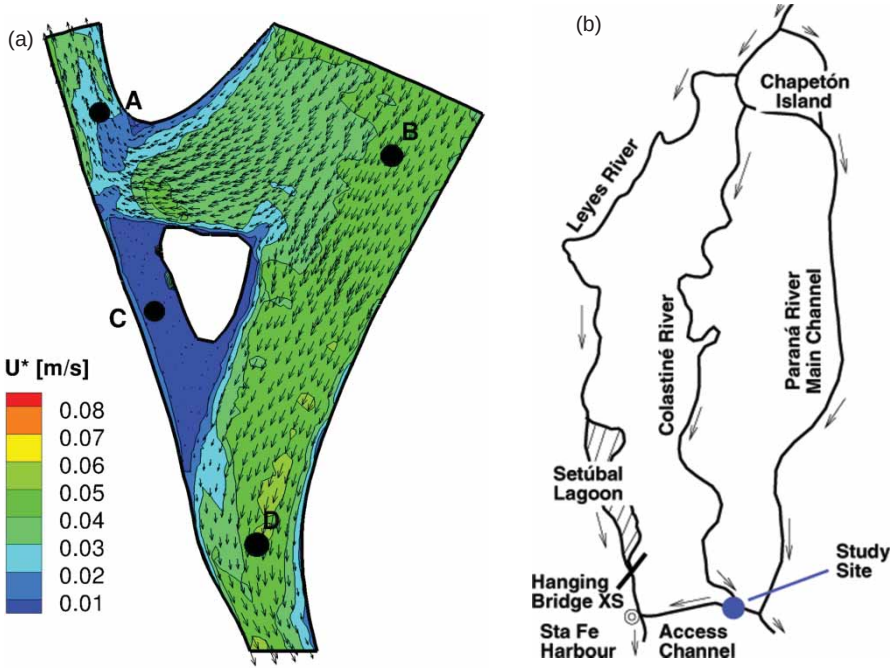

Figure 9. (a) Distribution of U_* and 2DH velocity field for the base state; (b) Sketch of the Leyes-Setúbal system upstream of Santa Fe City.

about 50% of the primary velocity component. Unfortunately, due to limitations of the postprocessing interface, it is not possible at this moment to extract the results from Telemac-3d following the same procedure used to treat the field data. However, and besides an optical effect due to the 3D projection algorithm used to plot the solution, the results along XS2 show a significant net unidirectional flow component in the transverse direction from outer to inner regions. It is the mass conservation constraint that triggers this transverse flow to compensate the accelerated flow that sets up along the inner regions of the bend. The contour values of the flow module points the region of accelerated flow.

Finally, Figure 9(a) plots the distribution of the 2DH velocity field obtained from the 3D computations. The solution captures the overall flow pattern inferred from the float paths shown in Figure 4(a). Both numerical and field data show a weakly curved flow field with almost parallel streamlines along the left branch.

3.3. *A feasible solution to the sedimentation problem of Santa Fe's harbour*

The cost of the maintenance dredging required to keep the access channel operational goes off the current ship toll system ruling the navigation of commercial vessels along the Paraná main channel from Santa Fe to the Atlantic Ocean. This additional cost, afforded by the Santa Fe Province, has put the local harbour in a disadvantageous position since the 1970s. Nevertheless, there is one possible solution that could deliver the basis for a new, cost-effective alternative to turning around this disadvantage.

It is technical feasible to close the South Derivation Channel ("Canal de Derivacion Sur", pt.(d), Figure 1) in order to reverse the flow direction in the access channel. The partial closure of the South Derivation Channel – an ecological downstream discharge must be kept – can divert enough water to set up an unidirectional flow through the external reach of the access channel. The strength of this unidirectional flow should be able to keep most of the transported sand particles up in suspension. Local people reported having witnessed the flow reversal phenomena along the access channel during some of the extreme floods experienced by the Paraná River on the twentieth century (Vionnet et al. 2006), albeit there is no record of such inversion.

Figure 9(b) sketches the 1D network of the so-called Leyes-Setúbal system, a complex anabranch system of the Paraná main channel. It has its origin nearby the Colastiné mouth and receives part of the Colastiné discharge through the access channel. Due to the lack of systematic discharge records along the Leyes-Setúbal system, it is quite reasonable to assume a mean flow through it on the order of 2400 $m^3 s^{-1}$. Such estimate is the outcome of assuming an average flow velocity between 0.8 and 1 ms^{-1} with an approximated wetted area of 2400–3000 m^2 along the Hanging Bridge cross-section (300 m wide and 8–10 m depth, see Figure 9(b) for the bridge XS location). Notwithstanding further hydrological and morphological studies

Table 4. U_*[ms^{-1}] for the different flow scenarios in the access channel.

Q [m^3 s^{-1}]	585	−500	−700	−900	−1100
A	0.019	0.018	0.027	0.035	0.043
B	0.045	0.047	0.047	0.047	0.047
C	0.004	0.056	0.064	0.073	0.081
D	0.047	0.078	0.082	0.087	0.089

are necessary if the proposed solution is eventually considered, there seems to be enough water available to divert part of it through the access channel.

The constructed numerical model with Telemac-3d is the natural starting point to test the proposed solution. The contour values of the bed shear velocity U_*, computed for the base state (the scenario reported from Figures 7 to 9(a)), along with 4 testing points located within the study area are detailed in Figure 9(a). Point A is located at the access channel mouth, where the strength of the secondary currents is maximum, point B upstream in the Colastiné River, point C in the middle of the external reach of the access channel, and point D downstream, on the thalweg of the bifurcation left branch.

Figure 9(a) includes not only the contour values of U_* in the background but also the 2DH velocity vectors distribution on top of it. Table 4 summarizes the computed values of U_* in the testing points when the boundary condition at the outflow of the right downstream branch is changed from free to a prescribed flow condition. The negative values of Q stands for the new inflow boundary conditions whereas the positive value of 585 m^3 s^{-1} corresponds to the base scenario. Figure 10(a) shows the counterpart of Figure 9(a) when the outflow boundary condition at the inlet of the access channel is set to the prescribed inflow value $Q = -1100\,\mathrm{m^3\,s^{-1}}$.

The large, low-gradient sandy-bed Paraná River moves its bed material as both bedload and suspended load, albeit suspended load far dominates bedload (Amsler et al. 2005). Strictly speaking, the separation between both transport modes is not a sharp process. Nonetheless, two criteria are widely used to estimate the onset of initiation of motion and initiation of suspension. The criteria used to quantify the onset of motion of grains of a non-cohesive sediment bed, and the onset of significant suspension of bed material are the Shields diagram and the Bagnold approximation, respectively. The Shields curve reads

$$\frac{U_*^2}{gRD} = 0.22\,\mathrm{Re_p^{-0.6}} + 0.06 \times 10^{-7.7\mathrm{Re_p^{-0.6}}}, \qquad (2)$$

after Brownlie (1981), for any river bed composed of grains of characteristic size D and submerged specific gravity R, where $\mathrm{Re_p}$ is a particle Reynolds number defined by the expression

$$\mathrm{Re_p} = \frac{\sqrt{gRD}D}{\nu}. \qquad (3)$$

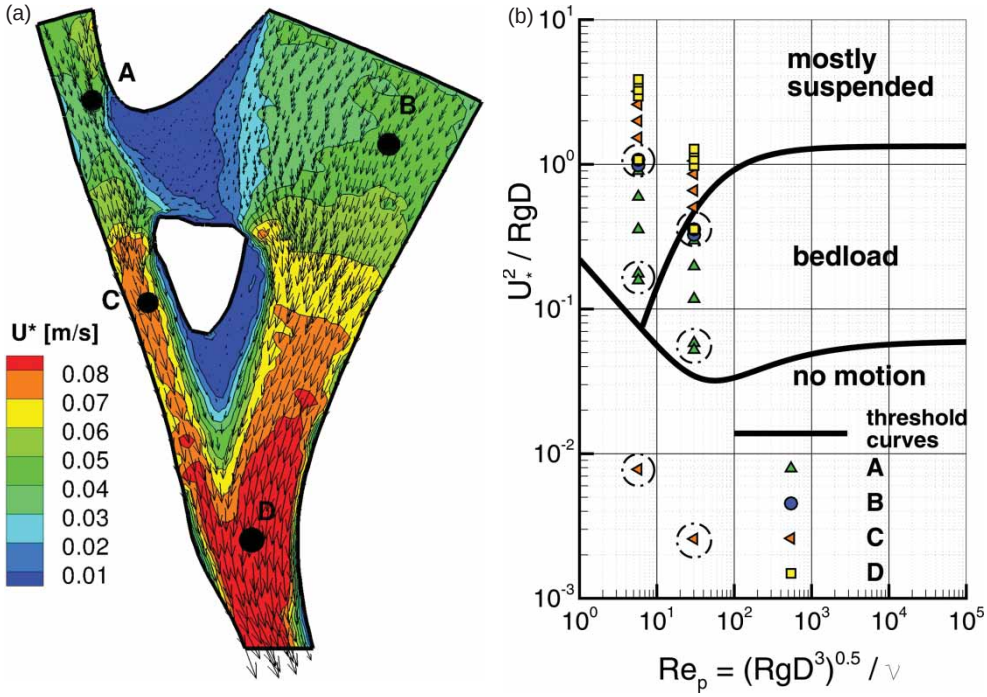

Figure 10. (a) Distribution of U_* and 2DH velocity field for $Q = -1100\,\mathrm{m^3\,s^{-1}}$; (b) Shield's diagram; the encircled points represent the dominant sediment transport modes for the base flow situation summarized in Table 4 (first column) for the size range [127–384] μm of bed particles.

Here, g is the acceleration due to gravity and ν the kinematic viscosity of water that is approximately 1.0×10^{-6} m^2 s^{-1} at 20°C. The so-called Bagnold criteria, a standard rule of thumb commonly accepted to define the onset of significant suspension, is defined by

$$\frac{U_*}{W_s} \simeq 1, \tag{4}$$

where W_s is the particle fall velocity, usually computed as an empirical function of the grain diameter, the acceleration due to gravity, and the kinematic viscosity of water.

Now, the prevailing sediment transport modes along the four testing points can be inferred from a diagram of U_*^2/gRD vs. $\mathrm{Re_p}$. Figure 10(b) depicts the threshold curves defined by Equations (2) and (4) with few isolated points summarizing the flow conditions of Table 4, for a particle size range that goes plus-minus one standard deviation from the geometric mean size $D_g = 221\,\mu$m (Figure 2(c)). This range covers almost 70% of all sediment sizes sampled at the study site, under the assumption that the grain distribution can be well approximated with a Gaussian function.

The points encircled in Figure 10(b) represent the dominant sediment transport modes for the base flow situation along the testing locations. The prevailing conditions at point C are of no sediment motion for both ends of the sediment size range considered. Any particle within that size range that reaches the neighbourhood of C either as bedload or suspended load is going to remain nearby without moving any further. On the other testing sites, the prevailing transport mode is suspended for the lower range of sediment size and mixed for the upper range.

However, the situation changes drastically when the flow along the access channel is reversed, notably in point C. All sediment particles within the tested range is going to be transported mostly in suspension except in the vicinity of point A, where bedload would still be dominant. The situation improves around point D and there are no signs of changes upstream of the diffluence, in the vicinity of point B. The prevailing bedload transport condition around point A would deactivate if the actual right branch is closed up to the mid-channel island. The low values of U_* (Figure 10(a)) between the actual right riverbank and the mid-channel island clearly shows that the future left branch – under the flow reversal scenario – would be part of an unstable diffluence (or part of an evolving confluence). It seems only a matter of time before the river ends up closing the branch. Consequently, the eventual closure of both the South Derivation Channel and the actual right branch of the diffluence surely warrant the setup of a self-dredging flow turning the actual diffluence into a stable confluence node.

4. Conclusions

Float paths produced on the study site, and numerical results obtained with Telemac, confirm the presence of a central core of convectively accelerated flow bounded by curved streamlines along both branches of the diffluence. The flow along the left branch is smooth, weakly curved, whereas the flow along the right branch exhibit regions of flow stagnation, separation and reattachment.

Field data captured with the Sontek ADCP, and processed with an in-house code show that the right branch contains a well-defined central cell of secondary currents. Although absent here, TRDI ADCP data show the same secondary motion. The helicoidal flow formed along the right branch keeps a scour hole at the access channel mouth. There, the channel sharp turn provokes the separation of the incoming boundary layer and, therefore, the formation of a vertical axis vortex at the curve apex. All these features are well captured by the 2D and 3D numerical solutions, including the observed free-surface deflection along the diffluence head whose "piecewise" shape is in tune with the expected flow behaviour.

River discharge data processed with the in-house software is consistent with the proprietary ADCP software, a required validation step before inferring the presence of secondary currents. Unfortunately, a unified algorithm to isolate cross-flow from a skewed discharge produced with either numerical or field data are still lacking. In particular, no unbiased algorithm is yet available to project the 3D computed velocity field onto selected cross-sections. The mentioned limitation hampers the users to judge the capability of Telemac-3d to capture secondary currents along river bends. The group is developing the user interface to extract the numerical data from Telemac-3d to project them onto any cross-section with the same algorithm embedded in the software developed to treat field data.

According to the produced field measurements, the hydrodynamics of the studied bifurcation has remained essentially unaltered during the observation period. Initially, it was possible to spot zones of stagnant water around the sandbar driving the flow along circular streamlines, a role later occupied by the emerged mid-channel island. However, and despite the recent changes seen during the study period, the reconstructed morphology of the site along a century-long record establishes the stability of the riverbanks surrounding the bifurcation node at the access channel mouth. The node initially conformed to a Y-shaped bifurcation, later evolved to a T-shaped, and recently underwent a transitional stage towards a Y-shaped node with a bifurcation angle γ close to the stability range reported by Federici and Paola (2003). How much of this convergence is due to recent changes of the Colastiné River hydrology, or to a natural process, is beyond the scope of this paper. Finally, the numerical outputs for the flow reversal scenario along the access channel show that the sedimentation problem experienced by the Santa Fe

City harbour is solvable. The closure of both the South Derivation Channel and the actual right branch of the diffluence surely warrant the set-up of a self-dredging flow (such that most transported sediment carry in suspension) turning the actual diffluence into a stable confluence node.

While the local authorities decided to move the harbour to the point (e), FICH (1998) recommended doing so nearby point (f) (Figure 1). The reasons why the local harbour authorities ignored to explore the South Derivation Channel closure in occasion of the FICH (1998) studies are not clear to the authors. Around 2008, part of the harbour facilities had been turned into a commercial complex gathering a hotel-casino with a shopping mall. Nevertheless, the commercial complex is far away from the loading/unloading areas. The closure of the South Derivation Channel could provide not only the required self-dredging flow along the access channel but also several hundreds of metres for ship docking and additional space for good's storage.

Acknowledgements

Part of this work was supported by the CONICET under Grant 11220100100384. Financial support from EDF and UNL is also gratefully acknowledged. Special thanks are given to Jean-Michel Hervouet for his support, to Carlos Ramonell who kindly provided the historical charts used for reconstructing the morphological evolution of the study site, and to two anonymous reviewers for their useful criticisms.

Supplemental data

Supplemental data for this article can be accessed http://dx.doi.org/10.1080/23249676.2014.981371.

Notes on contributors

Mariana I Morell is a Ph.D. student in water resources engineering at the Engineering and Water Resources, Departement (FICH) at the Universidad Nacional del Litoral (UNL), Santa Fe, Argentina. Her current research interest focuses on 3D modelling of confluence–diffluence units and field measurements.

Pablo A Tassi obtained his M.Sc. degree from FICH in 2001, and later moved to the University of Twente, Enschede, The Netherlands, to get his Ph.D. degree in computational mechanics. He is currently Ingénieur Chercheur at EDF (Electricité de France).

Carlos A Vionnet got his Ph.D. degree in mechanical engineering at the Department of Aerospace and Mechanical Engineering at the University of Arizona, Tucson, Arizona, USA. He is currently involved in modelling free-surface flows in river meanders and environmental data processing.

References

Amsler MA, Ramonell CG, Toniolo HA. 2005. Morphologic changes in the Paraná river channel (Argentina) in the light of the climate variability during the 20th century. Geomorphology. 70:257–278.

Babuska I, Rheinboldt WC. 1978. Error estimates for adaptive finite element computations. SIAM J Numer Anal. 15(4):735–754.

Bathurst JC, Thorne CR, Hey RD. 1979. Secondary flow and shear stress at river bends. J Hydraul Div ASCE. 105(10):1277–1295.

Blanckaert K, de Vriend HJ. 2004. Secondary flow in sharp open-channel bends. J Fluid Mech. 498:353–380.

Bolla Pittaluga M, Repetto R, Tubino M. 2003. Channel bifurcation in braided rivers: equilibrium configurations and stability. Water Resour Res. 39(3). doi:10.1029/2001WR001112

Brownlie WR. 1981. Prediction of flow depth and sediment discharge in open channels. Report KH-R-43A. Pasadena (CA): W. M. Keck Laboratory of Hydraulics and Water Resources, California Institute of Technology.

Burge LM. 2006. Stability, morphology and surface grain size patterns of channel bifurcation in gravel-cobble bedded anabranching rivers. Earth Surf Process Landf. 31:1211–1226.

Dargahi B. 2004. Three-dimensional flow modelling and sediment transport in the River Klaralven. Earth Surf Process Landforms. 29:821–852.

Dietrich WE, Smith JD. 1983. Influence of the point bar on flow through curved channels. Water Resour Res. 19(5):1173–1192.

Dinehart RL, Burau JR. 2005. Averaged indicators of secondary flow in repeated acoustic Doppler current profiler crossings of bends. Water Resour Res. 41(W09405). doi:10.1029/2005WR004050

Engelund F. 1974. Flow and bed topography in channel bends. J Hydraul Div ASCE. 100(11):1631–1648.

Federici B, Paola C. 2003. Dynamics of channel bifurcations in noncohesive sediments. Water Resour Res. 39(6):1162–1176. doi:10.1029/2002WR001434

FICH. 1998. Análisis preliminar de alternativas de ubicación de posibles terminales complementarias del Puerto de Santa Fe. Final Rep., Comisión Administr. Prov. Ente Puerto de Santa Fe, FICH-UNL, Santa Fe, Argentina.

Hervouet JM. 2007. Free surface flows: modelling with the finite element method. Chichester: Wiley.

Iriondo MH. 2007. Chapter 2: geomorphology. In: Iriondo M, Paggi J, Parma M, editors. The middle Paraná river: Limnology of a subtropical wetland. Berlin: Springer-Verlag; p. 33–52.

Johannesson H, Parker G. 1989. Secondary flow in mildly sinuous channel. J Hydraul Eng. 115(3):289–308.

Kashyap S, Constantinescu G, Rennie CD, Post G, Townsend R. 2012. Influence of channel aspect ratio and curvature on flow, secondary circulation, and bed shear stress in a rectangular channel bend. J Hydraul Eng. 138:1045–1059.

Kleinhans MG, Jagers HRA, Mosselman E, Sloff CJ. 2008. Bifurcation dynamics and avulsion duration in meandering rivers by one-dimensional and three-dimensional models. Water Resour Res. 44(W08454). doi:10.1029/2007WR005912

Lane SN, Bradbrook KF, Richards KS, Biron PM, Roy AG. 1999. Time-averaged flow structure in the central region of a stream confluence: a discussion. Earth Surf Process Landforms. 24:361–367.

Lievens A. 1997. The river plate experience; maintenance dredging by means of privatisation. Terra et Aqua. 68: 3–10.

Lloyd P, Stansby P. 1997. Shallow-water flow around model conical islands of small side slope. II: submerged. J Hydraul Eng. 123(12):1068–1077.

Miori S, Hardy RJ, Lane SN. 2012. Topographic forcing on flow partition and flow structures at river bifurcations. Earth Surf Process Landforms. 37:669–679.
Muste M, Yu K, Spasojevic M. 2004. Practical aspects of ADCP data use for quantification of mean river flow characteristics; part I: moving-vessel measurements. Flow Meas Instrum. 15(1):1–16. ISSN 0955–5986
Parsons DR, Jackson PR, Czuba JA, Engel FL, Rhoads BL, Oberg KA, Best JL, Mueller DS, Johnson KK, Riley JD. 2013. Velocity mapping toolbox (VMT): a processing and visualization suite for moving-vessel adcp measurements. Earth Surf Processes Landforms. 38:1244–1260.
Ramonell C. 2012. Evaluación de procesos hidro-geomorfológicos del Río Paraná entre los ejes del Arroyo Leyes y Santa Fe-Paraná. Final Rep. Sectei 21-18-10, Argentina: FICH-UNL, Santa Fe State Gov.
Rhoads BL, Kenworthy ST. 1998. Time-averaged flow structure in the central region of a stream confluence. Earth Surf Processes Landforms. 23:171–191.
Rhoads BL, Kenworthy ST. 1999. On secondary circulation, helical motion and Rozovskii-based analysis of time-averaged two-dimensional velocity fields at confluences. Earth Surf Process Landf. 24:369–375.
Richardson WR, Thorne CR. 2001. Multiple thread flow and channel bifurcation in a braided river: Brahmaputra–Jamuna river, Bangladesh. Geomorphology. 38:185–196.
Rozovskii IL. 1957. Flow of water in bends of open channels (in Russian). Kiev: Izd. Akad. Ukr. SSR. Israel Program for Sci. Transl., 1961, Jerusalem, 1957.
Simpson MR. 2001. Discharge measurements using a broad-band acoustic doppler current profiler. Open-File Report 01-1 1395. Sacramento (CA): USGS.
SMS. 2000. Surface modeling system. User's manual. UT: EMRL, Brigham Young University.
Snyder JP. 1929. Map projections – a working manual. Profess. Paper 1395. Washington (DC): USGS.
Sontek. 2004. Riversurveyor system manual. Software version 4.10. San Diego (CA): SonTek/YSI Inc.
Szupiany RN, Amsler ML, Best JL, Parsons DR. 2007. Comparison of fixed- and moving-vessel flow measurements with an adp in a large river. J Hydraul Eng. 133(12):1299–1309. doi:10.1061/(ASCE)0733-9429(2007)133:12(1299)
Szupiany RN, Amsler ML, Parsons DR, Best JL. 2009. Morphology, flow structure, and suspended bed sediment transport at two large braid-bar confluences. Water Resour Res. 45(W05415).
Tecplot. 2011. Tecplot 360TM version 2011. User's manual. Bellevue (WA): Tecplot Inc.
Telemac-Mascaret Modelling System. 2014. Webpage. Available from: http://www.opentelemac.org
TRDI. 2007. WinRiver II. User's guide. Poway (CA): Teledyne RD Instruments.
Vionnet CA. 2010. River bed topography; interpolation of scatter data. Internal Rep. 01-2010. Santa Fe (Argentina): Centre for Water and Enviromental Studies – CENEHA, FICH-UNL.
Vionnet CA, Tassi PA, Martin-Vide JP. 2004. Estimates of flow resistance and eddy viscosity coefficients for 2D modelling on vegetated floodplains. Hydrol Process. 18:2907–2926. doi:10.1002/hyp.5596
Vionnet CA, Tassi PA, Rodríguez LB, Ferreira CG. 2006. Numerical modelling of the catastrophic flooding of Santa Fe City, Argentina. Int J River Basin Manag. 4(4):301–314.
de Vriend H, Geldof H. 1983. Main flow velocity in short river bends. J Hydraul Eng. 109(7):991–1011. doi:10.1061/(ASCE)0733-9429(1983)109:7(991)
Yalin MS, editor. 1992. River mechanics. Oxford: Pergamon Press Ltd.

Appendix. Independent computation of river discharge

If the vessel path encloses a region Ω of boundary $\partial\Omega$, characterized by the unit tangent vector $\mathbf{t} = (t_x, t_y) \equiv (\delta x/\delta s, \delta y/\delta s)$ and the negative unit normal vector $\mathbf{n}^- = (-\delta y/\delta s, \delta x/\delta s)$, obtained through a 90° counterclockwise rotation from $\mathbf{t}$, where the positive direction of $\mathbf{t}$ points in the direction of increasing arc-length (s^+) when the path is traversed in the counterclockwise direction (such that the interior of the enclosed region Ω is on the left), a simple relation for the mass continuity can be derived. In the absence of any sources or sinks, the mass conservation constraint for a steady shallow-water flow of depth-averaged horizontal velocity $\mathbf{U} = (U, V)$ and water layer thickness H reads $\nabla \cdot H\mathbf{U} = 0$, which can be converted into a line integral along four pieces of the boundary $\partial\Omega$: one across the channel going from left to right bank (which provides the sought discharge Q), two along both river banks (equal to zero due to the non-flux condition), and the final one across the channel in reversed direction (equal to $-Q$), i.e.

$$Q = \int_0^B (H\mathbf{U}) \cdot \mathbf{n}^+ \, \mathrm{d}s \simeq \sum_{j=1}^{n} F_j \, \overline{\Delta s_j}, \tag{A1}$$

where n refers to the number of ensembles or vertical profiles measured by the ADCP along the polyline (transect) of length B (not necessary equal to the channel width), Δs_j the separation distance between the j th and $j + 1$th ensembles (or profiles) and

$$\begin{aligned} F_j &= (UHt_y - VHt_x)_j, \\ \overline{\Delta s_j} &= \frac{(\Delta s_{j-1} + \Delta s_j)}{2}, \quad j = 1, \ldots, n. \end{aligned} \tag{A2}$$

Above, Δs_0 and Δs_n are the specified user distance from both river banks to the first and last measured ensemble, respectively, and $\mathbf{U} \cdot \mathbf{n}^+ = U_n$ represents the outward normal of the depth-averaged flow component (Figure A.1(a)).

The ADCP set-up divides each water column into n_b depth cells, variable along the transect according to the local water depth. In turn, the ADCP determines the magnitude and direction of the flow velocity at each depth cell, whose geographical coordinates ENU equates with the local planar and vertical (x, y, z) coordinates. Therefore, if (u, v, w) are the local planar and vertical velocity components estimated by the ADCP at the barycentric point (x, y, z) of each depth cell, the 2DH flow velocity components adopted here at every ensemble along the transect are

$$U = \frac{\sum_{i=1}^{n_b} u_i}{n_b + 1}, \quad V = \frac{\sum_{i=1}^{n_b} v_i}{n_b + 1}, \tag{A3}$$

which results from imposing the no-slip condition at the river bed. Moreover, the use of Equation (A3) in Equation (A2) implicitly assumes that the upper layer of unmeasured water (due to blanking distance and transducer draft) and the bottom layer moves with the mean velocity $\mathbf{U} = (U, V)$ (Figure A.1(a)). The trapezoid rule for approximating the definite integral (5) amounts to estimate the lateral unmeasured portions of the cross-section as $Q_{\text{left}} = F_1 \Delta s_0/2$ and $Q_{\text{right}} = F_n \Delta s_n/2$ (Figure A.1(b)).

It must be clear that the procedures implemented in the in-house code to approximate the surface-nearest and bed-nearest velocity values within an ADCP profile, and the discharge values near the river banks as well, differ greatly from the one-sixth power-law and the ratio interpolation methods embedded in the

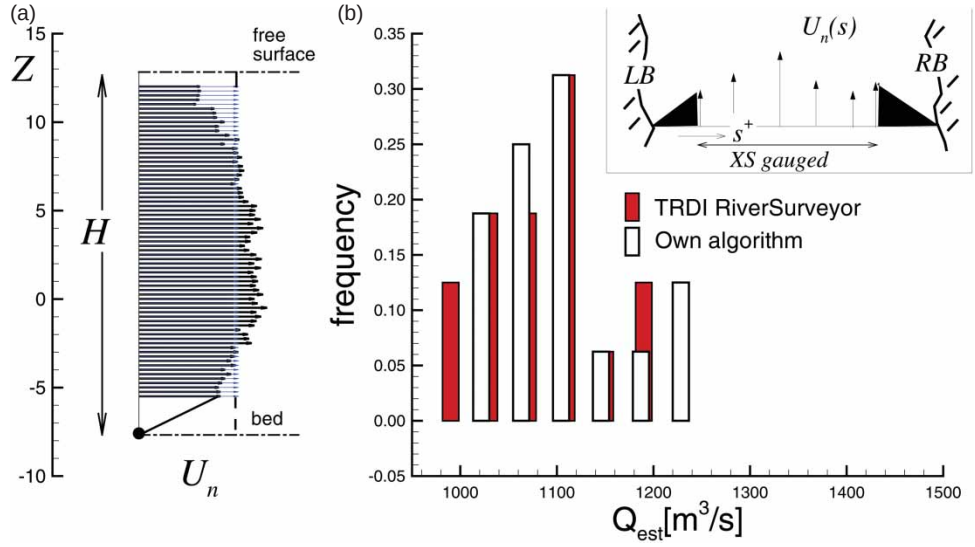

Figure A.1. River discharge as computed by *read_aDcp*. (a) variable arrows: actual velocity measurements, constant arrows: mean velocity according to Equation (7) projected in normal direction, (b) frequency distribution computed by the proprietary software and by the in-house user interface.

proprietary software (Simpson 2001; Sontek 2004; TRDI 2007). Nevertheless, Figure A.1(b) shows that the river discharge values computed with *read_aDcp* and with the proprietary ADCP software compare favourably well as explained in the text.

In any real-time data collection situation, the differential distance traversed by the boat in the elapsed time δt_j is $\delta s_j = V_b \delta t_j$, where V_b is the mean vessel velocity in the time period δt_j. Consequently, the above expression for the river discharge can be rearranged into the scalar triple product

$$Q = \int_0^{T(B)} (\mathbf{U}H \times \mathbf{t}V_b) \cdot \mathbf{k}\, \mathrm{d}t, \qquad \text{(A4)}$$

where $\mathbf{k}$ is the unit vector in the upward direction, t the time, and $T(B)$ the elapsed time required to traverse the transect path along the cross-section. A similar equation comprises the moving-vessel methodology for measuring total discharge using an ADCP (Simpson 2001; TRDI 2007). Here, the expression (A1) is used instead to verify if the actual cross-section data were surveyed from the left bank to the right bank ($Q < 0$), or vice-versa ($Q > 0$). For the latter case, the ADCP surveyed data is reversed, so both left and right banks are correctly located when observing data from upstream to downstream as it is customary in fluvial hydraulics. In the meantime, Equation (A1) also provides an independent estimate of the river discharge.